NANO LETTERS

pubs.acs.org/NanoLett

Letter

Synergistic Effect of Ionic Liquid and Embedded QDs on 2D Ferroelectric Perovskite Films with Narrow Phase Distribution for Self-Powered and Broad-Band Photodetectors

Linjuan Guo, Xiaoran Yang, Yu Liang, Zihao Wu, Xingyuan San, Zhenguang Wang, Leipeng Li, Zhenyang Liu, Jianhui Chen, Shufang Wang, Xuning Zhang,* Caofeng Pan,* and Zheng Yang*

Cite This: *Nano Lett.* 2024, 24, 11599−11606

Read Online

ACCESS | Metrics & More | Article Recommendations | Supporting Information

ABSTRACT: 2D layered metal halide perovskites (MHPs) are a potential material for fabricating self-powered photodetectors (PDs). Nevertheless, 2D MHPs produced via solution techniques frequently exhibit multiple quantum wells, leading to notable degradation in the device performance. Besides, the wide band gap in 2D perovskites limits their potential for broad-band photodetection. Integrating narrow-band gap materials with perovskite matrices is a viable strategy for broad-band PDs. In this study, the use of methylamine acetate (MAAc) as an additive in 2D perovskite precursors can effectively control the width of the quantum wells (QWs). The amount of MAAc greatly affects the phase purity. Subsequently, PbSe QDs were embedded into the 2D perovskite matrix with a broadened absorption spectrum and no negative effects on ferroelectric properties. PM6:Y6 was combined with the hybrid ferroelectric perovskite films to create a self-powered and broad-band PD with enhanced performance due to a ferro-pyro-phototronic effect, reaching a peak responsivity of 2.4 A W^{-1} at 940 nm.

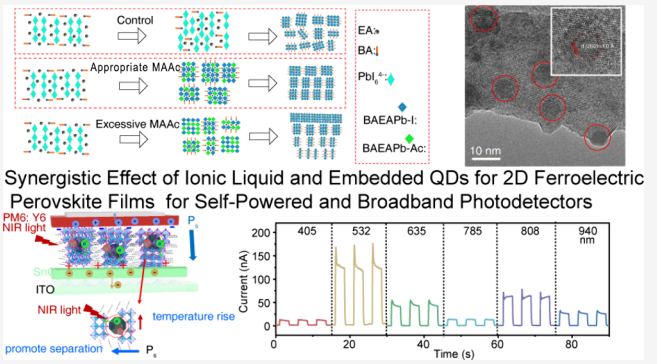

KEYWORDS: *2D perovskite ferroelectrics, phase purity regulation, ionic liquid, PbSe QDs, tandem-like self-powered photodetectors*

Self-powered photodetectors (PDs) are suitable for low-energy optoelectronic applications in industries, environmental monitoring, and military applications because they do not need external power sources, have wireless capabilities, and last a long time.[1−6] Broad-band PDs have potential in autonomous driving, food security monitoring, machine vision, and biometric identification, unlike UV and visible-light PDs.[7−10] Metal halide perovskites (MHPs) are beneficial in a range of optoelectronic applications, including photovoltaics, light-emitting diodes (LEDs), X-ray imaging, lasers, and PDs.[11−14] The structural formula for two-dimensional (2D) MHPs can be represented as $L_2A_{n-1}M_nX_{3n+1}$ (Ruddlesden−Popper) or $L'A_{n-1}M_nX_{3n+1}$ (Dion−Jacobson), where L represents the monoamine ligand and L′ represents the diamine ligand. A denotes small cations, such as Cs^+, and M represents Pb^{2+}, Sn^{2+}, or Ge^{2+}. X represents a halide, and *n* represents the number of inorganic layers formed by the MX_6 octahedron between two long chains, resulting in a natural quantum well (QW). In contrast to three-dimensional (3D) MHPs characterized by diminished stability, 2D layered MHPs are more stable and flexible and have potential ferroelectricity, making them a promising material for optoelectronic devices.[15−17] Ferroelectric MHPs are seen as promising for high-performance, self-powered PDs because of their strong spontaneous polarization, unlike traditional MHPs.[18−20]

2D MHPs made using solution methods often have multiple quantum wells (MQWs) with varying widths, which can greatly reduce device performance.[21] Also, precise control of phase purity is crucial for achieving strong ferroelectric properties.[22] High phase purity in 2D perovskites improves the carrier transport and stability. Various methods, including using additives like *n*-butylamine acetate instead of *n*-butylamine iodide, can enhance phase purity in 2D MHPs.[23] Qin et al. successfully obtained 2D perovskite films with high phase purity using a technique involving specific solvents (dimethylacetamide, toluene, and hydroiodic acid (HI) as nonpolar cosolvents) to control phase purity.[24] Zhao et al. employed HI as an additive to modulate the phase distribution of quasi-2D perovskite by facilitating the formation of PbI_3^-

Received: July 3, 2024
Revised: August 29, 2024
Accepted: August 29, 2024
Published: September 4, 2024

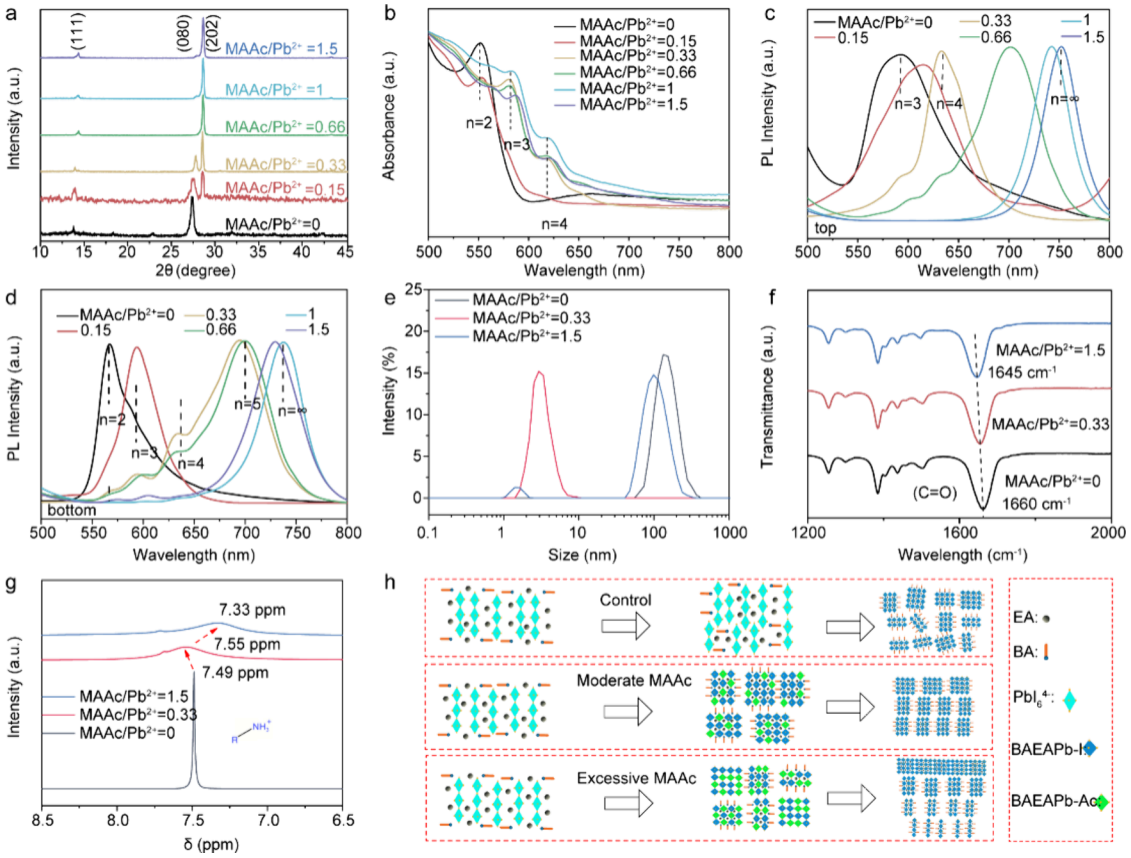

Figure 1. Influence of the MAAc content on the properties of $BA_2EA_2Pb_3I_{10}$ films. (a) XRD patterns, (b) absorption spectra, and steady-state PL spectra excited from (c) the top side and (d) the bottom side of the $MAAc_0$, $MAAc_{0.15}$, $MAAc_{0.33}$, $MAAc_{0.66}$, $MAAc_1$, and $MAAc_{1.5}$ perovskite films. (e) Dynamic light scattering shows the particle size distributions in the precursor solutions containing different MAAc contents. (f) The transmission FTIR of precursor solutions containing different MAAc contents. (g) ^{1}H NMR spectra of the perovskite solutions containing different MAAc contents by dissolving the precursors with DMSO-d_6. (h) Schematic illustration of the crystallization process in the solution without MAAc, with moderate MAAc, and excess MAAc.

complexes.[25] More research is needed to understand how the additives' contents affect phase distribution despite their effective modulation. 2D perovskites have a wide optical bandgap, limiting their ability to absorb UV−visible light for photodetection in the NIR band. To address this, the pyro-phototronic effect (PPE), which relies on temperature-induced changes in polarization, is a promising method to expand the response spectrum of PDs.[26] Weak NIR absorption in 2D perovskites limits their potential for improved photodetection through multiphoton absorption and pyroelectricity, resulting in low NIR pyroelectric responses due to hot carriers causing lattice temperature increases.[27−32] Integrating narrow-bandgap materials into perovskite matrices is a viable strategy for high-performance broad-band PDs.[33] PbX (X = S, Se) quantum dots embedded in a perovskite matrix show exceptional stability and a broadened light absorption spectrum and combine the benefits of both materials.[34−37] However, different bandgap values and band positions can lead to a type-I band alignment between QDs and perovskites.[38] The creation of a quantum well trapped excitons in quantum dots, leading to more recombination instead of charge carrier separation. This was demonstrated in PDs using PbS QDs in $MAPbI_{2.5}B_{r0.5}$, where a large external bias was needed for electron−hole separation through mechanisms like tunneling or emission over a barrier, integrating them into the perovskite phase.[39] To improve self-powered and broad-band PDs with QDs in perovskites, efficient charge extraction from the QDs to the perovskite matrix is crucial. A strong built-in electric field is needed to reduce carrier recombination during charge transfer, which can be enhanced by spontaneous polarizations in photoferroelectrics for effective separation of photogenerated carriers.[40,41] Furthermore, forming a tandem-like architecture with perovskite and NIR near-infrared absorption organic material can further result in a high-performance broad-band response.[42]

This study first demonstrates the preparation of a ferroelectric quasi-2D perovskite film ($BA_2EA_2Pb_3I_{10}$, BA = butylamine and EA = ethylamine) coupled with PbSe QDs. MAAc was chosen as an additive in the precursors to control the QW width of 2D perovskite films. The MAAc content greatly affects the phase distribution. Adding PbSe QDs to the 2D perovskite matrix did not harm the ferroelectric characteristics and improved phase purity. Additionally, PM6:Y6 near-infrared absorbing material was combined with ferroelectric perovskite films to create a self-powered PD with improved performance due to the ferro-pyro-phototronic effect, with a peak responsivity of 2.4 A W^{-1} and a detectivity of 1.65×10^{14} jones at 940 nm. This study suggests a promising method for controlling the phase purity and lays the groundwork for developing self-powered PDs with 2D perovskites.

High-quality $BA_2EA_2Pb_3I_{10}$ (a ferroelectric material) perovskite films were produced by using a one-step constant

https://doi.org/10.1021/acs.nanolett.4c03143
Nano Lett. 2024, 24, 11599−11606

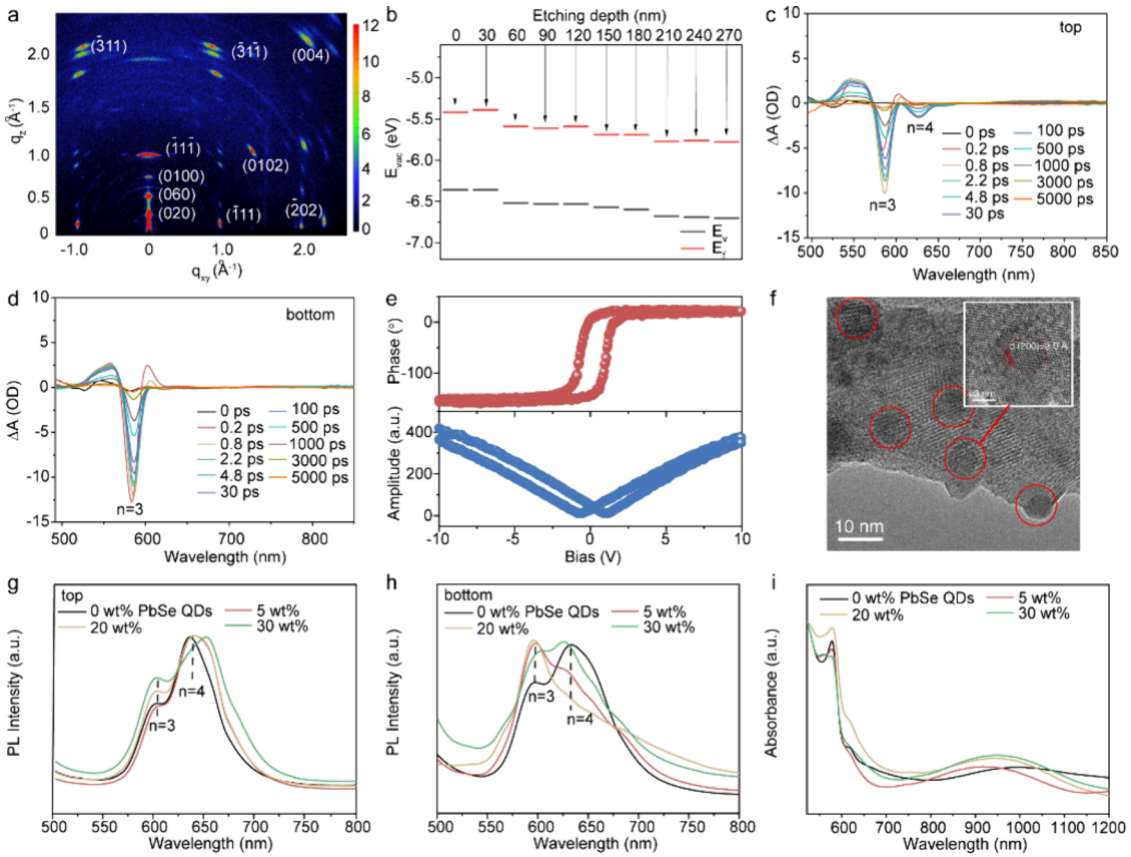

Figure 2. Characterizations of the $BA_2EA_2Pb_3I_{10}$-$MAAc_{0.33}$ film with/without QDs. (a) GIWAXS patterns of the $MAAc_{0.33}$ film. (b) Energy level diagram of the $MAAc_{0.33}$ film with different etching depths (from 0 to 270 nm). The TA spectra of $MAAc_{0.33}$ film excited from the (c) top side and (d) bottom side. (e) Out-of-plane PFM hysteresis loops measured in the film surface, showing an obvious hysteresis loop and butterfly curve. (f) HRTEM images of $(BA)_2EA_2Pb_3I_{10}$-$MAAc_{0.33}$ film with 20 wt % PbSe QDs. Steady-state PL spectra excited from the (g) top side and (h) bottom side of the $(BA)_2EA_2Pb_3I_{10}$-$MAAc_{0.33}$ films with different PbSe QDs mass fractions, showing an improvement of phase purity. (i) Absorption spectra of the four perovskite films.

temperature heating spin-coating method with different MAAc concentrations. Ac^- was used to control the crystallization of 2D perovskite by interacting strongly with Pb^{2+} ions, leading to effective regulation of crystal orientation and well width. Different MAAc/Pb^{2+} ratios (0, 0.15, 0.33, 0.66, 1, and 1.5) were tested to study the appearance and morphology of quasi-2D perovskite films. The films were labeled with $MAAc_0$, $MAAc_{0.15}$, $MAAc_{0.33}$, $MAAc_{0.66}$, $MAAc_1$, and $MAAc_{1.5}$. The color change from bright orange to dark red in Figure S1 indicates a shift in the phase distribution due to increased MAAc content. The perovskite films have smooth surfaces and large grain sizes, making them ideal for optoelectronic devices (Figure S2). The $MAAc_{0.33}$ film had the largest grain size. XRD analysis in Figure 1a shows that the film without MAAc has four distinct diffraction peaks. The main peak can be attributed to the (080) crystal plane of the 2D perovskite, with no peak from the (202) plane. More MAAc content led to increased film crystallinity, shown by dominant peaks from the (111) and (202) planes. The study found that perovskite films with MAAc had a preferred orientation and high quality. Various optical techniques like absorption spectra and photoluminescence spectra (PL) shown in Figure 1b–d were used to analyze the phase purity of the films, showing that $MAAc_0$ had a broad phase distribution. Adding a small amount of MAAc narrows the phase distribution, resulting in fewer observable exciton peaks. Specifically, for $MAAc_{0.33}$ film, only two exciton peaks for $\langle n \rangle = 3$ and $\langle n \rangle = 4$ are observable. However, a further increase in MAAc content leads to the emergence of additional 2D phases spanning from $n = 1$ to $n = \infty$ ($MAAc_1$ and $MAAc_{1.5}$ films). PL results from both the bottom and top were consistent with the absorption results. For $MAAc_{0.33}$ film, primary PL peaks correspond to phases with low n values (2 and 3). As the MAAc content increases, PL peaks shift to higher n values. The $MAAc_{0.33}$ film exhibits a primary PL peak at 595 nm for $n = 3$, adjacent to the ferroelectric phase. PL peaks corresponding to higher n values were observed in $MAAc_{0.66}$, $MAAc_1$, and $MAAc_{1.5}$ films, particularly in relation to unstable 3D-like phases induced by pseudohalide anions like SCN^-.[43] Next, we examined how the phase purity is affected by changing the MAAc levels. We measured the particle size distributions of the precursor solutions by using dynamic light scattering. Without MAAc, the average size of the colloids in the control perovskite precursors was 140 nm, indicating aggregation of PbI_6^{4-} octahedra. Adding a moderate amount of MAAc (MAAc/Pb^{2+} = 0.33) results in a smaller size distribution (3 nm) due to the strong interaction between Ac^- and Pb^{2+}. Increasing the MAAc content resulted in larger particles (98 nm) and multiple phases. A moderate MAAc content is best for high phase purity in 2D perovskite films with a uniform particle size. Transmission Fourier-transform infrared (FTIR) spectra of precursor solutions with different MAAc concentrations confirmed a strong interaction between Ac^- and Pb^{2+}. Figure 1f demonstrates that the C═O vibration peak in the control solution shifted to higher frequencies when

https://doi.org/10.1021/acs.nanolett.4c03143
Nano Lett. 2024, 24, 11599−11606

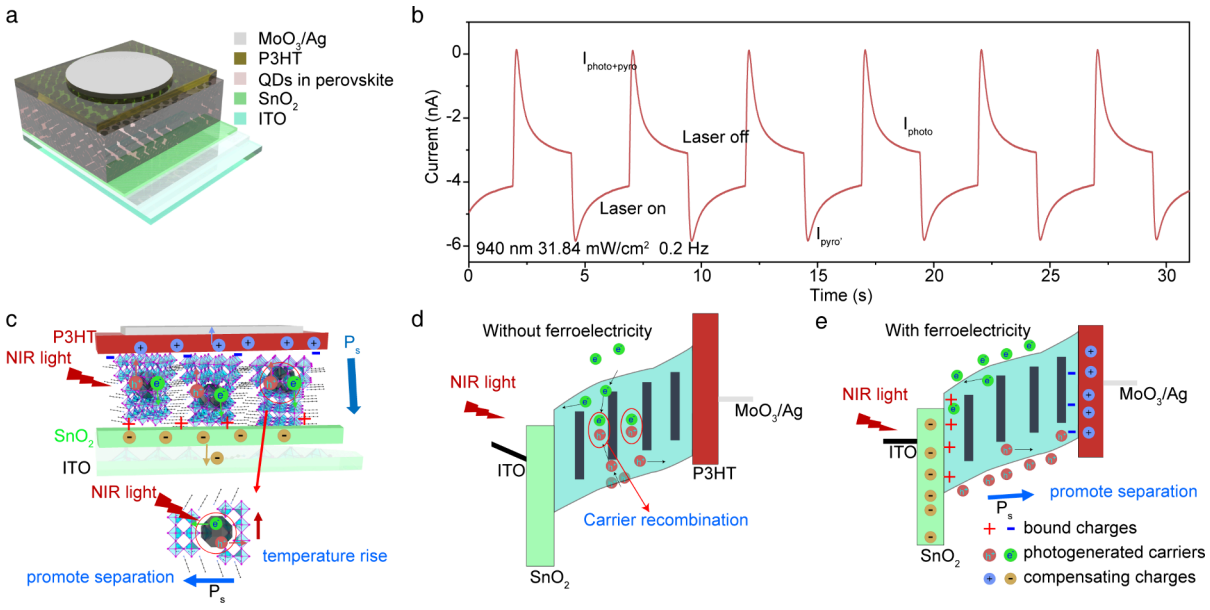

Figure 3. Working mechanism and comparison of the 2D perovskite-based PDs with/without PbSe QDs. (a) Schematic diagram showing the device structure with PbSe QDs. (b) *I*–*t* characteristics of the PD under a 940 nm laser, showing typical FPPE-induced responses. (c) Schematic diagram of the fundamental working mechanism of IPPE-based self-powered PDs under NIR light. Energy band diagrams of the self-powered PD based on hybrid films (d) without ferroelectricity and (e) with ferroelectricity under NIR illumination conditions.

MAAc was introduced, indicating the release of solvent molecules from the Pb^{2+} centers due to the strong interaction between Ac^- and Pb^{2+}. ^1H nuclear magnetic resonance (^1H NMR) spectra were used to analyze the chemical interactions between MAAc and precursor ions. In the presence of MAAc, a peak at 7.49 ppm for $-NH_3^+$ protons shifted slightly lower and decreased in intensity, likely due to increased shielding between amino and carboxyl groups. Higher MAAc levels led to downfield chemical shifts. Uniform precursor size and phase distribution can be achieved with moderate Ac^- complexation, but excessive MAAc can create phases with large *n* values. Figure 1h shows the crystallization process where adding MAAc creates a high-purity quasi-2D perovskite film due to strong Ac^- and Pb^{2+} interactions preventing aggregation of octahedra. This leads to a more uniform distribution of the intermediate phase in the solution. The last films were mostly made of 3D elements as the MAAc content increased. Excessive Ac^- during the intermediate phase may help create the 3D perovskite structure. This method also worked in three other quasi-2D perovskite films (Figure S3–S5), namely $BDA_{0.7}BA_{0.6}EA_2Pb_3Br_{10}$ (BDA = butanediamine), $BA_2FA_2Pb_3I_{10}$ (FA = formamidine), and $PEA_2EA_2Pb_3Br_{10}$ (PEA = phenylethylamine). To better understand the role of the ionic liquid in regulating the 2D phase, another ionic liquid, methylamine formate (MAFa), and glacial acetic acid (HAc) were introduced to the precursor solution as additives containing Ac^-. As shown in Figure S4, MAFa can also modulate the phase distribution of the $BA_2EA_2Pb_3I_{10}$ perovskite films, similar to the results obtained with MAAc. Increasing the HAc content did not significantly affect the quasi-2D perovskite films' phase purity, as shown in Figure S5. As an ionic liquid with a high boiling point (158.2 °C), MAAc possesses negligible vapor pressure during the whole spin-coating procedure (90 °C).[44] Therefore, Ac^- in MAAc or Fa^- in MAFa can regulate crystallization effectively without being affected by heat, while HAc may easily evaporate from the solution before crystallization.

Then, the $MAAc_{0.33}$ film with high quality and high purity was chosen for PD fabrication, followed by a detailed analysis of its properties. The presence of MA^+ in the perovskite lattice was confirmed by using ^1H NMR spectroscopy (Figure S6), with a MA^+ to EA^+ molar ratio of 7:1. The crystal orientation of the $MAAc_{0.33}$ film was determined by using grazing-incidence wide-angle X-ray scattering (GIWAXS), showing sharp signals resembling ellipses for various crystal planes, indicating a vertical orientation that benefits charge carrier transport (Figure 2a). For the $MAAc_0$ film, diffraction rings were found, indicating the randomness of the crystal orientation (Figure S7). Ultraviolet photoelectron spectroscopy (UPS) measurements of the three different samples in Figure 2b and Figure S8 were conducted to evaluate the energy level distribution in the $MAAc_{0.33}$ film. The results show that within the top 30 nm, two energy levels remain almost constant, suggesting a phase of $n = 4$. Etching the film reveals a gradual decrease in energy level, with minimal changes in the Fermi level and valence band, indicating a phase of $n = 3$. The corresponding UPS and X-ray photoelectron spectra (XPS) are shown in Figures S9 and S10. The transient absorption (TA) spectra confirm the purity of the $MAAc_{0.33}$ film when excited from both sides (Figure 2c,d, Figure S11a–d). The lower *n* phase ($n = 3$) is at the bottom and the higher *n* phase ($n = 4$) is at the top, with the ferroelectric phase ($n = 3$) being the main phase in the $MAAc_{0.33}$ film. However, for $MAAc_0$ film, three bleaching peaks corresponding to $n = 2$, 3, and 4 were found for both top and bottom excitation conditions (Figure S12), indicating that the films obtained without MAAc have worse crystal orientation and phase distribution. The low trap densities (1.57×10^{13} cm^{-3} for electrons and 1.598×10^{13} cm^{-3} for holes) can be attributed to the introduction of Ac^- (Figure S11e,f). Piezoresponse force microscopy (PFM) tests confirmed the ferroelectric properties of the $MAAc_{0.33}$ film, as shown in Figure 2e and Figure S14. Phase and amplitude loops obtained through out-of-plane PFM demonstrated the polarization switching of ferroelectric domains. Subsequently, the

https://doi.org/10.1021/acs.nanolett.4c03143
Nano Lett. 2024, 24, 11599−11606

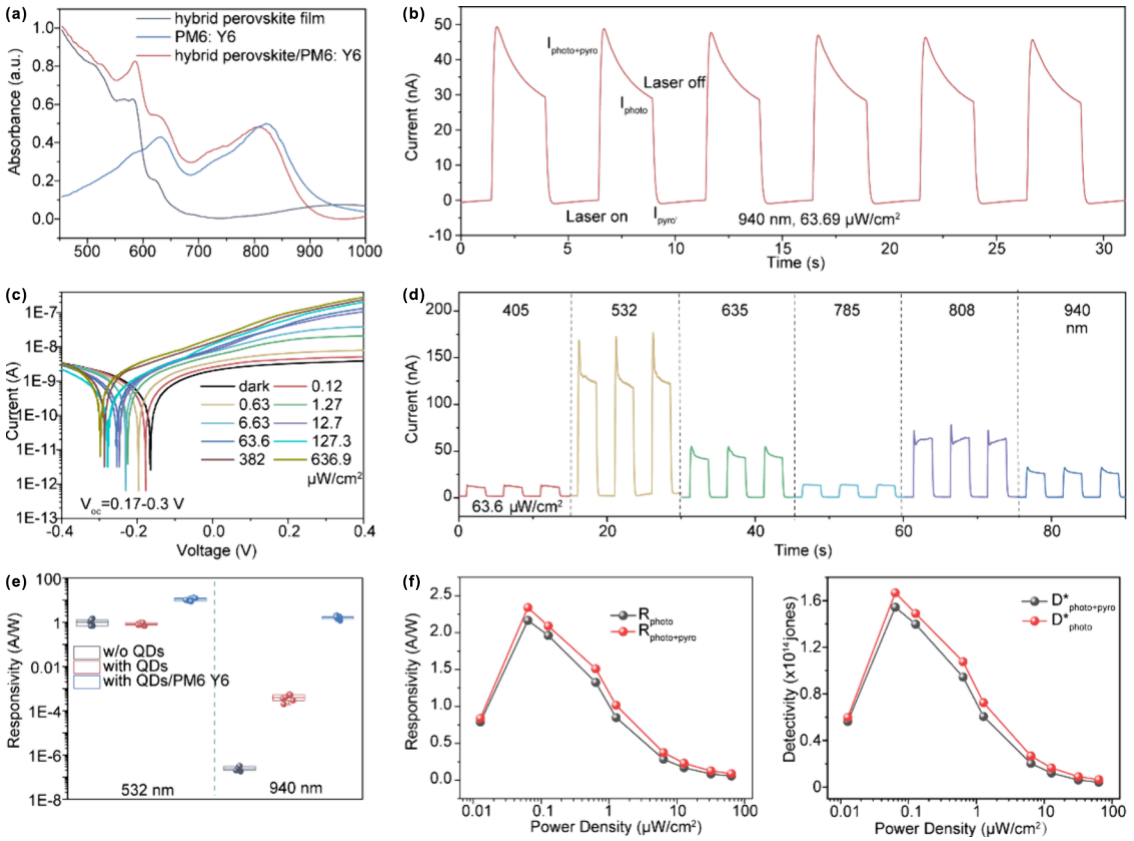

Figure 4. (a) Absorption spectra of the bare hybrid perovskite film, PM6:Y6 film, and tandem-like film. (b) $I-t$ characteristics of the PD under 940 nm laser, showing typical FPPE-induced four-stage responses. (c) $I-V$ curves of the PD under a 940 nm laser with different power densities, showing obvious V_{oc} ranging from 0.17 to 0.3 V. (d) Spectral photoresponse of the PDs under different light illuminations from 405 to 940 nm with same power density at 0 V bias. (e) Comparison of responsivities of three PDs (without QDs, with 20 wt % QDs, and QDs coupled with PM6:Y6). (f) Responsivities and (g) corresponding detectivities of the tandem-like PD as a function of the power density.

$(BA)_2EA_2Pb_3I_{10}$-$MAAc_{0.33}$ film devoid of PbSe QDs was initially employed to create PDs with a conventional n-i-p photovoltaic architecture (ITO/SnO_2/perovskite/P3HT/MoO_3/Ag), with detailed results being given in Figures S15−S26. The photoresponses depicted in Figures S22−S26 exhibit the distinct photodetection behaviors induced by the ferro-pyrophototronic effect (FPPE), which are subject to an operating bias, polarization direction, polarization voltage, operating temperature, and switching frequency. The above five factors can greatly influence the pyroelectric peaks.

The aforementioned bare PD had weak response currents because of the limited absorption range of the quasi-2D perovskite. Therefore, PbSe QDs were selected due to their narrow bandgap and compatibility with lead iodine perovskites. The PbSe QDs had an average size of 3.55 nm and an absorption cutoff at 1100 nm (Figures S27 and S28). Embedding PbSe QDs into the $BA_2EA_2Pb_3I_{10}$ perovskite lattice was achieved using spin coating. Different hybrid films named as films with 0 wt % PbSe QDs, with 5 wt % PbSe QDs, with 20 wt % PbSe QDs, and with 30 wt % PbSe QDs were created with varying amounts of PbSe QDs, affecting the morphologies, crystallinities, and optical properties of the films (Figures S29−S32), with a best mass fraction of 20 wt %. The crystal structure of PbSe QDs in the perovskite matrix for the 20 wt % sample was characterized using an high resolution transmission electron microscopy (HRTEM) image, showing evenly distributed QDs within the matrix. There were no noticeable differences in spacing between the QDs (a = 6.0 Å) and perovskites (a = 6.3937 Å, with a lattice mismatch of ∼6%), indicating an epitaxial alignment at the interface. The enhancement of phase purity was observed to increase as the intensity ratio of the PL peak for n = 3 to n = 4 increased (Figure 2g,h). This improvement was further confirmed by preparing $(BDA)_{0.7}(BA)_{0.6}EA_2Pb_3Br_{10}$ and $(BA)_2FA_2Pb_3I_{10}$ films with 20 wt % PbSe QDs in Figure S33, showing the universality of this strategy. PbSe QDs can serve as seed crystals and regulate the crystallization procedure for the 2D perovskite. Increasing QDs in the $BA_2MA_2Pb_3I_{10}$ film results in stronger absorption in the near-infrared region (Figure 2i). The QDs content increases from the bottom to the top of the 2D perovskite film (Figures S34 and S35), with more QDs located at the top surface of the hybrid film. The inclusion of PbSe QDs in the hybrid film can enhance the phase purity, thereby ensuring the presence of ferroelectricity (Figures S36 and S37).

Next, the 2D perovskite films with varying QD contents were used to construct PDs as depicted in Figure 3a and Figure S38. Figure 3b demonstrates the typical four-stage response behaviors when the samples are subjected to 940 nm laser illumination (0 V, 31.81 mW cm^{-2}). The photoresponses show consistent and stable results. Figure 3c illustrates how the FPPE operates. When a bias voltage is applied, positive charges are generated at the perovskite-SnO_2 interface and negative charges are generated at the perovskite-P3HT interface. Holes in P3HT and electrons in SnO_2 act as compensatory charges to maintain the electrical balance. Depletion layers at the interface

https://doi.org/10.1021/acs.nanolett.4c03143
Nano Lett. 2024, 24, 11599−11606

prevent compensatory charges from recombining with bound charges. Laser activation causes photoexcitation and carrier thermalization, leading to positive peak pyroelectric current flow and photocurrent. This combined current, $I_{photo+pyro}$, is due to a decrease in the ferroelectric polarization intensity. Continued illumination results in a steady temperature, leaving behind solely a platform of photocurrent (I_{photo}). After the laser was turned off, the perovskite films cooled and regained their ferroelectric polarization, leading to the production of a negative pyroelectric current (I_{pyro}'). The ferroelectricity-induced bulk photovoltaic effect, along with pyroelectric characteristics, is crucial for self-powered photodetection. PbSe QDs dominate light absorption under 940 nm illumination. Efficient charge carrier extraction is essential for PD performance, as a nonferroelectric perovskite leads to significant recombination rather than transportation and collection of holes and electrons by electrodes (Figure 3d), leading to limited output currents. The electric field from spontaneous polarization helps separate electrons and holes, allowing them to move across the quantum well boundaries and generate photocurrent in the perovskite material (Figure 3e).

The addition of 20 wt % PbSe QDs improves photoresponses, response speed, and stability compared to the bare PDs without QDs (Figures S39−S51). However, the maximum values for R and D^* under a 940 nm laser are determined to be 0.56 mA W^{-1} and 8.8 × 10^{10} jones, respectively, which are still much weaker than those for 532 nm. Therefore, a narrow-bandgap organic PM6:Y6 film replacing P3HT was directly desposited on the perovskite film to form a tandem-like structure. From Figure 4a, compared with the bare hybrid perovskite films, PM6:Y6 can expand the device's absorption spectrum from 650 to nearly 1000 nm. As shown in Figure 4b with a four-stage response to 940 nm laser light (0 V, 63.69 μW cm^{-2}), the photoresponses exhibit a notable level of repeatability and stability. Also, the introduction of PM6:Y6 can obviously enhance the temperature rise of the PD when illuminated with red and near-infrared lasers (Figures S52 and S53), leading to much higher pyroelectric photoresponses. Figure 4c shows the $I-V$ characteristics of the tandem-like PD under a 940 nm laser, with obvious open-circuit optical voltages (V_{oc}) ranging from 0.17 to 0.3 V, indicating a self-powered photodetection ability. Both the spectral photoresponses of the tandem-like PDs in Figure 4d and the averaged maximum responsivities of the three PDs (without QDs, with 20 wt % QDs, and with 20 wt % QDs coupled with PM6:Y6) in Figure 4e prove that the performances were greatly improved by a combination of QD insertion and integration with PM6:Y6. The detailed performances of the tandem-like PDs are shown in Figures S54−S57. R and D^* were estimated to be 2.4 A W^{-1} and 1.65 × 10^{14} jones (at 0.1 μW cm^{-2}), respectively (Figure 4f,g). The performance of our PDs and those of previously reported perovskite coupled with narrow-band-material-based PDs are compared in Table S1, showing that our PDs demonstrate relatively higher photoresponsivity and detectivity and comparable response/recovery times. Moreover, most of those PDs are nonself-powered ones, proving the advantage of our strategy.

In summary, the introduction of thr ionic liquid MAAc (a moderate mount of Ac^-:Pb^{2+} = 0.33) effectively controls the phase distribution of 2D perovskite films, resulting in high-quality ferroelectric films. Further addition of PbSe QDs improved the phase purity, absorption spectral range of the epitaxially grown 2D perovskite matrix, and overall stabilities, while maintaining the ferroelectric properties. PM6:Y6, a near-infrared absorbing material, was integrated with hybrid films to create a tandem-like self-powered PD. Based on the FPPE, the responsivities and response speed of the tandem-like PDs demonstrated a notable enhancement upon exposure to infrared laser (940 nm) irradiation, with a peak responsivity of 2.4 A W^{-1} and a detectivity of 1.65 × 10^{14} jones. The investigation's results offer a promising way to control phase purity and lay the groundwork for improving self-powered PDs based on 2D perovskites.

■ ASSOCIATED CONTENT

Supporting Information

The Supporting Information is available free of charge at https://pubs.acs.org/doi/10.1021/acs.nanolett.4c03143.

Experimental section of the whole process, equations of trap-state density, responsivity, and specific detectivity, characterizations of 2D perovskite films, characterizations of PbSe QDs and 2D perovskite films with QDs, detailed photoresponses of the self-powered PDs, and performance comparisons of reported broad-band photodetectors based on perovskites coupled with narrow-band materials (PDF)

■ AUTHOR INFORMATION

Corresponding Authors

Xuning Zhang − *Hebei Key Laboratory of Photo-Electricity Information and Materials, College of Physics Science and Technology, Hebei University, Baoding 071002, P. R. China*; Email: zhangxn@hbu.edu.cn

Caofeng Pan − *Institute of Atomic Manufacturing, Beihang University, Beijing 100191, P. R. China*; orcid.org/0000-0001-6327-9692; Email: pancaofeng@buaa.edu.cn

Zheng Yang − *Hebei Key Laboratory of Photo-Electricity Information and Materials, College of Physics Science and Technology and Institute of Life Science and Green Development, Hebei University, Baoding 071002, P. R. China*; orcid.org/0000-0001-7172-4717; Email: yangzheng06@hbu.edu.cn

Authors

Linjuan Guo − *Hebei Key Laboratory of Photo-Electricity Information and Materials, College of Physics Science and Technology, Hebei University, Baoding 071002, P. R. China*

Xiaoran Yang − *Hebei Key Laboratory of Photo-Electricity Information and Materials, College of Physics Science and Technology, Hebei University, Baoding 071002, P. R. China*

Yu Liang − *Hebei Key Laboratory of Photo-Electricity Information and Materials, College of Physics Science and Technology, Hebei University, Baoding 071002, P. R. China*

Zihao Wu − *Hebei Key Laboratory of Photo-Electricity Information and Materials, College of Physics Science and Technology, Hebei University, Baoding 071002, P. R. China*

Xingyuan San − *Hebei Key Laboratory of Photo-Electricity Information and Materials, College of Physics Science and Technology, Hebei University, Baoding 071002, P. R. China*

Zhenguang Wang − *Key Laboratory of Chemical Biology of Hebei Province, Key Laboratory of Medicinal Chemistry and Molecular Diagnosis, Ministry of Education, College of Chemistry and Materials Science, Hebei University, Baoding 071002, P. R. China*; orcid.org/0000-0003-2001-5165

https://doi.org/10.1021/acs.nanolett.4c03143
Nano Lett. 2024, 24, 11599−11606

Leipeng Li − *Hebei Key Laboratory of Photo-Electricity Information and Materials, College of Physics Science and Technology and Institute of Life Science and Green Development, Hebei University, Baoding 071002, P. R. China*
Zhenyang Liu − *Hebei Key Laboratory of Photo-Electricity Information and Materials, College of Physics Science and Technology, Hebei University, Baoding 071002, P. R. China;* orcid.org/0000-0002-8453-5744
Jianhui Chen − *Hebei Key Laboratory of Photo-Electricity Information and Materials, College of Physics Science and Technology, Hebei University, Baoding 071002, P. R. China*
Shufang Wang − *Hebei Key Laboratory of Photo-Electricity Information and Materials, College of Physics Science and Technology, Hebei University, Baoding 071002, P. R. China*

Complete contact information is available at: https://pubs.acs.org/10.1021/acs.nanolett.4c03143

Author Contributions

L.G. and X.Y. contributed equally. Z.Y. and C.P. conceived the research and supervised the project. L.G. and X.Y. prepared the perovskites and measured the optoelectronic properties. Y.L. and Z.W. prepared the QDs samples and performed AFM and PFM experiments. X.S. performed TEM. Z.L. and L.L. performed the PL experiments. Z.W. performed the dynamic light scattering measurements. J.C. and X.Z. synthesized and prepared PM6:Y6 samples. L.G. wrote the manuscript. Z.Y. and L.G. modified it. S.W., X.Z., and C.P. provided funding support and critical suggestions for this work. All the authors reviewed the manuscript.

Notes

The authors declare no competing financial interest.

■ ACKNOWLEDGMENTS

This work was supported by the National Natural Science Foundation of China (Grant Nos. U20A20166, 62005072, and 62104057), the Natural Science Foundation of Hebei Province (Grant No. E2021201016), Hebei Education Department (Grant No. BJK2022050), the Science and Technology Plan Project of Hebei Province (Grant Nos. 226Z1002G and 226Z1703G), the Research Innovation Team Project of Hebei University (IT2023A04), and Hebei Province Optoelectronic Information Materials Laboratory Performance Subsidy Fund Project (No. 22567634H).

■ REFERENCES

(1) Liu, W.; Lv, J. H.; Peng, L.; Guo, H. W.; Liu, C.; Liu, Y. L.; Li, W.; Li, L. F.; Liu, L. X.; Wang, P. Q.; Bodepudi, S. C.; Shehzad, K.; Hu, G. H.; Liu, K. H.; Sun, Z. P.; Hasan, T.; Xu, Y.; Wang, X. M.; Gao, C.; Y, B.; Duan, X. F. Graphene charge-injection photodetectors. *Nat. Electron.* **2022**, *5*, 281−288.
(2) Youngblood, N.; Chen, C.; Koester, S. J.; Li, M. Waveguide-integrated black phosphorus photodetector with high responsivity and low dark current. *Nat. Photonics* **2015**, *9*, 247−252.
(3) Koepfli, S. M.; Baumann, M.; Koyaz, Y.; Gadola, R.; Gungor, A.; Keller, K.; Horst, Y.; Nashashibi, S.; Schwanninger, R.; Doderer, M.; Passerini, E.; Fedoryshyn, Y.; Leuthold, J. Metamaterial graphene photodetector with bandwidth exceeding 500 gigahertz. *Science* **2023**, *380*, 1169−1174.
(4) Jia, C.; Wu, S.; Fan, J.; Luo, C.; Fan, M.; Li, M.; He, L.; Yang, Y.; Zhang, H. Ferroelectrically modulated and enhanced photoresponse in a self-powered alpha-In_2Se_3/Si heterojunction photodetector. *ACS Nano* **2023**, *17*, 6534−6544.
(5) Shen, K.; Xu, H.; Li, X.; Guo, J.; Sathasivam, S.; Wang, M.; Ren, A.; Choy, K. L.; Parkin, I. P.; Guo, Z.; Wu, J. Flexible and self-powered photodetector arrays based on all-inorganic $CsPbBr_3$ quantum dots. *Adv. Mater.* **2020**, *32*, No. 2000004.
(6) Hu, X.; Li, X. Y.; Li, G. Y.; Ji, T.; Ai, F. J.; Wu, J. H.; Ha, E.; Hu, J. Q. Recent progress of methods to enhance photovoltaic effect for self-powered heterojunction photodetectors and their applications in inorganic low-dimensional structures. *Adv. Funct. Mater.* **2021**, *31*, No. 2011284.
(7) Zhang, Y.; Vafaie, M.; Xu, J.; Pina, J. M.; Xia, P.; Najarian, A. M.; Atan, O.; Imran, M.; Xie, K.; Hoogland, S.; Sargent, E. H. Electron-transport layers employing strongly bound ligands enhance stability in colloidal quantum dot infrared photodetectors. *Adv. Mater.* **2022**, *34*, No. 2206884.
(8) Lee, C.; Xu, E. Z.; Kwock, K. W. C.; Teitelboim, A.; Liu, Y.; Park, H. S.; Ursprung, B.; Ziffer, M. E.; Karube, Y.; Fardian-Melamed, N.; Pedroso, C. C. S.; Kim, J.; Pritzl, S. D.; Nam, S. H.; Lohmueller, T.; Owen, J. S.; Ercius, P.; Suh, Y. D.; Cohen, B. E.; Chan, E. M.; Schuck, P. J. Indefinite and bidirectional near-infrared nanocrystal photoswitching. *Nature* **2023**, *618*, 951−958.
(9) Chen, D. K.; March, S. D.; Jones, A. H.; Shen, Y.; Dadey, A. A.; Sun, K. Y.; McArthur, J. A.; Skipper, A. M.; Xue, X. J.; Guo, B. T.; Bai, J. W.; Bank, S. R.; Campbell, J. C. Photon-trapping-enhanced avalanche photodiodes for mid-infrared applications. *Nat. Photonics* **2023**, *17*, 594−600.
(10) Chikkaraddy, R.; Arul, R.; Jakob, L. A.; Baumberg, J. J. Single-molecule mid-infrared spectroscopy and detection through vibrationally assisted luminescence. *Nat. Photonics* **2023**, *17*, 865−871.
(11) Chen, C.; Chen, J.; Han, H.; Chao, L.; Hu, J.; Niu, T.; Dong, H.; Yang, S.; Xia, Y.; Chen, Y.; Huang, W. Perovskite solar cells based on screen-printed thin films. *Nature* **2022**, *612*, 266−271.
(12) Han, D.; Wang, J.; Agosta, L.; Zang, Z.; Zhao, B.; Kong, L.; Lu, H.; Mosquera-Lois, I.; Carnevali, V.; Dong, J.; Zhou, J.; Ji, H.; Pfeifer, L.; Zakeeruddin, S. M.; Yang, Y.; Wu, B.; Rothlisberger, U.; Yang, X.; Gratzel, M.; Wang, N. Tautomeric mixture coordination enables efficient lead-free perovskite leds. *Nature* **2023**, *622*, 493−498.
(13) Kim, J.; Heo, J.; Park, G.; Woo, S.; Cho, C.; Yun, H.; Kim, D.; Park, J.; Lee, S.; Park, S.; Yoon, E.; Greenham, N.; Lee, T. W. Ultra-bright, efficient and stable perovskite light-emitting diodes. *Nature* **2022**, *611*, 688−694.
(14) Lin, R.; Wang, Y.; Lu, Q.; Tang, B.; Li, J.; Gao, H.; Gao, Y.; Li, H.; Ding, C.; Wen, J.; Wu, P.; Liu, C.; Zhao, S.; Xiao, K.; Liu, Z.; Ma, C.; Deng, Y.; Li, L.; Fan, F.; Tan, H. All-perovskite tandem solar cells with 3d/3d bilayer perovskite heterojunction. *Nature* **2023**, *620*, 994−1000.
(15) Blancon, J. C.; Even, J.; Stoumpos, C. C.; Kanatzidis, M. G.; Mohite, A. D. Semiconductor physics of organic-inorganic 2D halide perovskites. *Nat. Nanotechnol.* **2020**, *15*, 969−985.
(16) Qin, C.; Sandanayaka, A. S. D.; Zhao, C.; Matsushima, T.; Zhang, D.; Fujihara, T.; Adachi, C. Stable room-temperature continuous-wave lasing in quasi-2D perovskite films. *Nature* **2020**, *585*, 53−57.
(17) Hou, J.; Li, W. B.; Zhang, H.; Sidhik, S.; Fletcher, J.; Metcalf, I.; Anantharaman, S. B.; Shuai, X. T.; Mishra, A.; Blancon, J. C.; Katan, C.; Jariwala, D.; Even, J.; Kanatzidis, M. G.; Mohite, A. D. Synthesis of 2D perovskite crystals via progressive transformation of quantum well thickness. *Nat. Synth.* **2024**, *3*, 265−275.
(18) Li, X.; Zhang, F.; Yue, Z.; Wang, Q.; Sun, Z.; Luo, J.; Liu, X. Centimeter-size single crystals of halide perovskite photoferroelectric solid solution with ultrahigh pyroelectricity boosted photodetection. *Angew. Chem., Int. Ed. Engl.* **2023**, *62*, No. 2305310.
(19) Xu, H.; Sun, F.; Guo, W.; Han, S.; Liu, Y.; Fan, Q.; Tang, L.; Liu, W.; Luo, J.; Sun, Z. Building block-inspired hybrid perovskite derivatives for ferroelectric channel layers with gate-tunable memory behavior. *Angew. Chem., Int. Ed. Engl.* **2023**, *62*, No. 2309416.
(20) Han, S.; Li, L.; Ji, C.; Liu, X.; Wang, G. E.; Xu, G.; Sun, Z.; Luo, J. Visible-photoactive perovskite ferroelectric-driven self-powered gas detection. *J. Am. Chem. Soc.* **2023**, *145*, 12853−12860.
(21) Gu, H.; Xia, J. M.; Liang, C.; Chen, Y. H.; Huang, W.; Xing, G. C. Phase-pure two-dimensional layered perovskite thin films. *Nat. Rev. Mater.* **2023**, *8*, 533−551.

(22) Guo, L.; Qi, Y.; Wu, Z.; Yang, X.; Yan, G.; Cong, R.; Zhao, L.; Zhang, W.; Wang, S.; Pan, C.; Yang, Z. A self-powered UV photodetector with ultrahigh responsivity based on 2D perovskite ferroelectric films with mixed spacer cations. *Adv. Mater.* **2023**, *35*, No. 2301705.
(23) Liang, C.; Gu, H.; Xia, Y.; Wang, Z.; Liu, X.; Xia, J.; Zuo, S.; Hu, Y.; Gao, X.; Hui, W.; Chao, L.; Niu, T.; Fang, M.; Lu, H.; Dong, H.; Yu, H.; Chen, S.; Ran, X.; Song, L.; Li, B.; Zhang, J.; Peng, Y.; Shao, G.; Wang, J.; Chen, Y.; Xing, G.; Huang, W. Two-dimensional ruddlesden-popper layered perovskite solar cells based on phase-pure thin films. *Nat. Energy* **2021**, *6*, 38−45.
(24) Qin, Y.; Zhong, H. J.; Intemann, J. J.; Leng, S. F.; Cui, M. H.; Qin, C. C.; Xiong, M.; Liu, F.; Jen, A. K. Y.; Yao, K. Coordination engineering of single-crystal precursor for phase control in ruddlesden-popper perovskite solar cells. *Adv. Energy Mater.* **2020**, *10*, No. 1904050.
(25) Zhao, R.; Guo, L.; Zhu, H.; Zhang, T.; Li, P.; Zhang, Y.; Song, Y. Regulation of quantum wells width distribution in quasi-2D perovskite films for high-performance photodetectors. *Adv. Mater.* **2023**, *35*, No. 2301232.
(26) Dai, Y.; Wang, X.; Peng, W.; Xu, C.; Wu, C.; Dong, K.; Liu, R.; Wang, Z. L. Self-powered Si/CdS flexible photodetector with broadband response from 325 to 1550 nm based on pyro-phototronic effect: An approach for photosensing below bandgap energy. *Adv. Mater.* **2018**, *30*, No. 1705893.
(27) Fu, J.; Ramesh, S.; Melvin Lim, J. W.; Sum, T. C. Carriers, quasi-particles, and collective excitations in halide perovskites. *Chem. Rev.* **2023**, *123*, 8154−8231.
(28) Guo, L.; Liu, X.; Gao, L.; Wang, X.; Zhao, L.; Zhang, W.; Wang, S.; Pan, C.; Yang, Z. Ferro-pyro-phototronic effect in monocrystalline 2D ferroelectric perovskite for high-sensitive, self-powered, and stable ultraviolet photodetector. *ACS Nano* **2022**, *16*, 1280.
(29) Guo, L.; Wang, H.; Xu, Z.; Cong, R.; Zhao, L.; Zhang, S.; Zhang, K.; Gao, L.; Wang, S.; Pan, C.; Yang, Z. Interfacial pyro-phototronic effect: A universal approach for enhancement of self-powered photodetection based on perovskites with centrosymmetry. *Adv. Funct. Mater.* **2023**, *33*, No. 2306526.
(30) Guo, L.; Qi, Y.; Yang, Z.; Zhao, L.; Zhang, W.; Wang, X.; Liu, H.; Yan, G.; Wang, S.; Pan, C. 2D Ruddlesden-Popper perovskite ferroelectric film for high-performance, self-powered and ultra-stable UV photodetector boosted by ferro-pyro-phototronic effect and surface passivation. *Nano Energy* **2022**, *102*, No. 107714.
(31) Guo, L.; Liu, X.; Cong, R.; Gao, L.; Zhang, K.; Zhao, L.; Wang, X.; Wang, R. N.; Pan, C.; Yang, Z. Patterned 2d ferroelectric perovskite single-crystal arrays for self-powered uv photodetector boosted by combining ferro-pyro-phototronic and piezo-phototronic effects. *Nano Lett.* **2022**, *22*, 8241−8249.
(32) Yang, Z.; Wang, H.; Guo, L.; Zhou, Q.; Gu, Y.; Li, F.; Qiao, S.; Pan, C.; Wang, S. A self-powered photodetector based on $MaPbI_3$ single-crystal film/n-si heterojunction with broadband response enhanced by pyro-phototronic and piezo-phototronic effects. *Small* **2021**, *17*, No. 2101572.
(33) Mei, L.; Huang, R.; Shen, C.; Hu, J.; Wang, P.; Xu, Z.; Huang, Z.; Zhu, L. Hybrid halide perovskite-based near-infrared photodetectors and imaging arrays. *Adv. Opt. Mater.* **2022**, *10*, No. 2102656.
(34) Hosokawa, H.; Tamaki, R.; Sawada, T.; Okonogi, A.; Sato, H.; Ogomi, Y.; Hayase, S.; Okada, Y.; Yano, T. Solution-processed intermediate-band solar cells with lead sulfide quantum dots and lead halide perovskites. *Nat. Commun.* **2019**, *10*, 43.
(35) Liu, M.; Chen, Y.; Tan, C. S.; Quintero-Bermudez, R.; Proppe, A. H.; Munir, R.; Tan, H.; Voznyy, O.; Scheffel, B.; Walters, G.; Kam, A. P. T.; Sun, B.; Choi, M. J.; Hoogland, S.; Amassian, A.; Kelley, S. O.; Garcia de Arquer, F. P.; Sargent, E. H. Lattice anchoring stabilizes solution-processed semiconductors. *Nature* **2019**, *570*, 96−101.
(36) Ning, Z.; Gong, X.; Comin, R.; Walters, G.; Fan, F.; Voznyy, O.; Yassitepe, E.; Buin, A.; Hoogland, S.; Sargent, E. H. Quantum-dot-in-perovskite solids. *Nature* **2015**, *523*, 324−328.
(37) Gao, L.; Quan, L. N.; García de Arquer, F. P.; Zhao, Y.; Munir, R.; Proppe, A.; Quintero-Bermudez, R.; Zou, C.; Yang, Z.; Saidaminov, M. I.; Voznyy, O.; Kinge, S.; Lu, Z.; Kelley, S. O.; Amassian, A.; Tang, J.; Sargent, E. H. Efficient near-infrared light-emitting diodes based on quantum dots in layered perovskite. *Nat. Photonics* **2020**, *14*, 227−233.
(38) Chen, H.; Pina, J.; Hou, Y.; Sargent, E. Synthesis, applications, and prospects of quantum-dot-in-perovskite solids. *Adv. Energy Mater.* **2022**, *12*, No. 2100774.
(39) Garcia de Arquer, F.; Gong, X.; Sabatini, R.; Liu, M.; Kim, G.; Sutherland, B.; Voznyy, O.; Xu, J.; Pang, Y.; Hoogland, S.; Sinton, D.; Sargent, E. Field-emission from quantum-dot-in-perovskite solids. *Nat. Commun.* **2017**, *8*, 14757.
(40) Li, L.; Sun, Z.; Wang, P.; Hu, W.; Wang, S.; Ji, C.; Hong, M.; Luo, J. Tailored engineering of an unusual $(C_4H_9(NH_3)_2(CH_3NH_3)_2Pb_3Br_{10}$ two-dimensional multilayered perovskite ferroelectric for a high-performance photodetector. *Angew. Chem., Int. Ed. Engl.* **2017**, *56*, 12150−12154.
(41) Cao, F. R.; Tian, W.; Wang, M.; Cao, H. P.; Li, L. Semitransparent, flexible, and self-powered photodetectors based on ferroelectricity-assisted perovskite nanowire arrays. *Adv. Funct. Mater.* **2019**, *29*, No. 1901280.
(42) Ollearo, R.; Ma, X.; Akkerman, H. B.; Fattori, M.; Dyson, M. J.; van Breemen, A. J. J. M.; Meskers, S. C. J.; Dijkstra, W.; Janssen, R. A. J.; Gelinck, G. H. Vitality surveillance at distance using thin film tandem like narrowband near infrared photodiodes with light enhanced responsivity. *Sci. Adv.* **2023**, *9*, 9861.
(43) Hong, L.; Wang, Z. W.; Milic, J. V.; Avalos, C. E.; Zhang, W. H.; Ren, D.; Wang, C.; Carlsen, B.; Liu, Y. H.; Zakeeruddin, S. M.; Hagfeldt, A.; Wang, T.; Han, H. W.; Graetzel, M. Thiocyanate-mediated dimensionality transformation of low- dimensional perovskites for photovoltaics. *Chem. Mater.* **2022**, *34*, 6331−6338.
(44) Chao, L. F.; Xia, Y. D.; Li, B. X.; Xing, G. C.; Chen, Y. H.; Huang, W. Room-temperature molten salt for facile fabrication of efficient and stable perovskite solar cells in ambient air. *Chem.* **2019**, *5*, 995−1006.

https://doi.org/10.1021/acs.nanolett.4c03143
Nano Lett. 2024, 24, 11599−11606